

Warwick Electron Microscopy Datasets

Jeffrey M. Ede^{1,*}

¹University of Warwick, Department of Physics, Coventry, CV4 7AL, UK

*j.m.ede@warwick.ac.uk

ABSTRACT

Large, carefully partitioned datasets are essential to train neural networks and standardize performance benchmarks. As a result, we have set up new repositories to make our electron microscopy datasets available to the wider community. There are three main datasets containing 19769 scanning transmission electron micrographs, 17266 transmission electron micrographs, and 98340 simulated exit wavefunctions, and multiple variants of each dataset for different applications. To visualize image datasets, we have trained variational autoencoders to parameterize 64-dimensional multivariate normal distributions, which we cluster in two dimensions by t-distributed stochastic neighbor embedding. In addition, we have improved dataset visualization with variational autoencoders by introducing encoding normalization and regularization, adding an image gradient loss, and extending t-distributed stochastic neighbor embedding to account for encoded standard deviations. Our datasets, source code, pretrained models, and interactive visualization tools are openly available at <https://github.com/Jeffrey-Ede/datasets>.

1 Introduction

We have set up new repositories¹ to make our large new electron microscopy datasets available to both electron microscopists and the wider community. There are three main datasets containing 19769 experimental scanning transmission electron microscopy² (STEM) images, 17266 experimental transmission electron microscopy² (TEM) images and 98340 simulated TEM exit wavefunctions³. Experimental datasets represent general research and were collected by dozens of University of Warwick scientists working on hundreds of projects between January 2010 and June 2018. We have been using our datasets to train artificial neural networks (ANNs) for electron microscopy³⁻⁷, where standardizing results with common test sets has been essential for comparison. This paper provides details of and visualizations for datasets and their variants, and is supplemented by source code, pretrained models, and both static and interactive visualizations⁸.

Machine learning is increasingly being applied to materials science^{9,10}, including to electron microscopy¹¹. Encouraging scientists, ANNs are universal approximators¹² that can leverage an understanding of physics to represent¹³ the best way to perform a task with arbitrary accuracy. In theory, this means that ANNs can always match or surpass the performance of contemporary methods. However, training, validating and testing requires large, carefully partitioned datasets^{14,15} to ensure that ANNs are robust to general use. To this end, our datasets are partitioned so that each subset has different characteristics. For example, TEM or STEM images can be partitioned so that subsets are collected by different scientists, and simulated exit wavefunction partitions can correspond to Crystallography Information Files¹⁶ (CIFs) for materials published in different journals.

Most areas of science are facing a reproducibility crisis¹⁷, including artificial intelligence¹⁸. Adding to this crisis, natural scientists do not always benchmark ANNs against standardized public domain test sets; making results difficult or impossible to compare. In electron microscopy, we believe this is a symptom of most datasets being small, esoteric or not having default partitions for machine learning. For example, most datasets in the Electron Microscopy Public Image Archive^{19,20} are for specific materials and are not partitioned. In contrast, standard machine learning datasets such as CIFAR-10^{21,22}, MNIST²³, and ImageNet²⁴ have default partitions for machine learning and contain tens of thousands or millions of examples. By publishing our large, carefully partitioned machine learning datasets, and setting an example by using them to standardize our research, we aim to encourage higher standardization of machine learning research in the electron microscopy community.

There are many popular algorithms for high-dimensional data visualization²⁵⁻³² that can map N high-dimensional vectors $\{\mathbf{x}_1, \dots, \mathbf{x}_N\}$, $\mathbf{x}_i \in \mathbb{R}^u$ to low-dimensional vectors $\{\mathbf{y}_1, \dots, \mathbf{y}_N\}$, $\mathbf{y}_i \in \mathbb{R}^v$. A standard approach for data clustering in $v \in \{1, 2, 3\}$ dimensions is t-distributed stochastic neighbor embedding^{33,34} (tSNE). To embed data by tSNE, Kullback-Leibler (KL) divergence,

$$L_{\text{tSNE}} = \sum_i \sum_{j \neq i} p_{ij} \log \left(\frac{p_{ij}}{q_{ij}} \right), \quad (1)$$

between Gaussian distributed similarities in real space, p_{ij} , and heavy-tailed Student t-distributed similarities in an embedding

space, q_{ij} , is minimized by gradient descent³⁵. For symmetric tSNE³³,

$$p_{ij} = \frac{\exp\left(-\|\mathbf{x}_i - \mathbf{x}_j\|_2^2 / 2\alpha_j^2\right)}{\sum_{k \neq j} \exp\left(-\|\mathbf{x}_k - \mathbf{x}_j\|_2^2 / 2\alpha_j^2\right)}, \quad (2)$$

$$p_{ij} = \frac{p_{i|j} + p_{j|i}}{2N}, \quad (3)$$

$$q_{ij} = \frac{(1 + \|\mathbf{y}_i - \mathbf{y}_j\|_2^2)^{-1}}{\sum_{k \neq i} (1 + \|\mathbf{y}_k - \mathbf{y}_i\|_2^2)^{-1}}. \quad (4)$$

To control the amount of clustering, perplexities of $p_{i|j}$ for each j are adjusted to a user-provided value by fitting α_j . Perplexity, $\exp(H)$, is an exponential function of entropy, H , and most tSNE visualizations are robust to moderate changes to its value.

Feature extraction is often applied to decrease input dimensionality, typically to $u \lesssim 100$, before clustering data by tSNE. Decreasing input dimensionality can decrease data noise and computation for large datasets, and is necessary for some high-dimensional data as distances, $\|\mathbf{x}_i - \mathbf{x}_j\|_2$, used to compute p_{ij} are affected by the curse of dimensionality³⁶. For image data, a standard approach³³ to extract features is probabilistic^{37,38} or singular value decomposition³⁹ (SVD) based principal component analysis⁴⁰ (PCA). However, PCA is limited to linearly separable features. Other hand-crafted feature extraction methods include using a histogram of oriented gradients⁴¹, speeded-up robust features⁴², local binary patterns⁴³, wavelet decomposition⁴⁴ and other methods⁴⁵. The best features to extract for a visualization depend on its purpose. However, most hand-crafted feature extraction algorithms must be tuned for different datasets. For example, Minka’s algorithm⁴⁶ is included in the scikit-learn⁴⁷ implementation of PCA by SVD to obtain the optimal number of principal components to use.

More complicated nonlinear and dataset-specific features can be extracted with deep learning, increasing representational power. For instance, by using the latent space of an autoencoder^{48,49} (AE) or features before logits in a classification ANN⁵⁰. Indeed, we have posted AEs for electron microscopy with pre-trained models^{51,52} that could be improved. However, AE latent vectors can exhibit inhomogeneous dimensional characteristics and pathological semantics, limiting correlation between latent vectors and semantic differences. To encode well-behaved latent vectors suitable for clustering by tSNE, variational autoencoders⁵³ (VAEs) can be trained to parameterize multivariate probability distributions. Typically, VAEs are trained to parameterize multivariate normal distributions by minimizing KL divergence from standard normal distributions. Imposing priors on latent vectors helps to homogenize dimensional characteristics, and additive sampling noise results in generated image semantics that are correlated with latent features.

2 Dataset Visualization

To visualize datasets presented later in this paper, we trained VAEs shown in figure 1 to embed images downsampled to 96×96 in $u = 64$ dimensions before clustering in $v = 2$ dimensions by tSNE. Our VAE consists of two convolutional neural networks^{54,55} (CNNs): an encoder, E , and a generator, G . The encoder embeds batches of B input images, I , as mean vectors, $\{\mu_1, \dots, \mu_B\}$, and standard deviation vectors, $\{\sigma_1, \dots, \sigma_B\}$, to parameterize multivariate normal distributions. During training, input images are linearly transformed to have minimum and maximum values of 0 and 1, respectively, and we apply a random combination of flips and 90° rotations to augment training data by a factor of eight. The generator learns to cooperate with the encoder to output encoder inputs by sampling latent vectors, $\mathbf{z}_i = \mu_i + \sigma_i \varepsilon_i$, where $\mu_i = \{\mu_{i1}, \dots, \mu_{iu}\}$, $\sigma_i = \{\sigma_{i1}, \dots, \sigma_{iu}\}$, and $\varepsilon_i = \{\varepsilon_{i1}, \dots, \varepsilon_{iu}\}$ are random variates sampled from standard normal distributions, $\varepsilon_{ij} \sim N(0, 1)$. Each convolutional or fully connected layer is followed by batch normalization⁵⁶ then ReLU⁵⁷ activation, except the output layers of the encoder and generator. An absolute nonlinearity, $f(x) = |x|$, is applied to encode positive standard deviations.

Traditional VAEs learn to minimize a balance, λ_{MSE} , between mean squared errors (MSEs) of generated images and KL divergence from a multivariate standard normal distribution⁵³,

$$L_{\text{trad}} = \lambda_{\text{MSE}} \text{MSE}(G(\mathbf{z}), I) + \frac{1}{2Bu} \sum_{i=1}^B \sum_{j=1}^u \mu_{ij}^2 + \sigma_{ij}^2 - \log(\sigma_{ij}^2) - 1. \quad (5)$$

However, traditional VAE training is sensitive to λ_{MSE} ⁵⁸ and other hyperparameters⁵⁹. If λ_{MSE} is too low, the encoder will learn to consistently output $\sigma_{ij} \simeq 1$, limiting regularization. Else if λ_{MSE} is too high, the encoder will learn to output $\sigma_{ij} \ll |\mu_{ij}|$, limiting regularization. As a result, traditional VAE hyperparameters must be carefully tuned for different ANN architectures and datasets. To improve VAE regularization and robustness to different datasets, we normalize encodings parameterizing

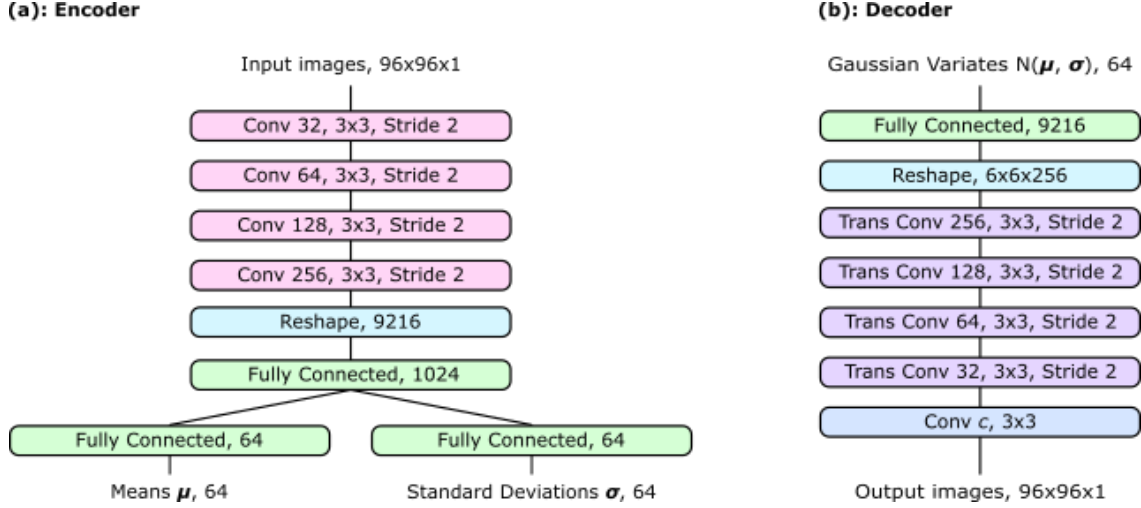


Figure 1. Simplified VAE architecture. a) An encoder outputs means, μ , and standard deviations, σ , to parameterize multivariate normal distributions, $\mathbf{z} \sim N(\mu, \sigma)$. b) A generator predicts input images from \mathbf{z} .

normal distributions to

$$\mu_{ij} \leftarrow \frac{\lambda_{\mu}(\mu_{ij} - \mu_{\text{avg},j})}{\mu_{\text{std},j}}, \quad (6)$$

$$\sigma_{ij} \leftarrow \frac{\sigma_{ij}}{2\sigma_{\text{std},j}}, \quad (7)$$

where batch means and standard deviations are

$$\mu_{\text{avg},j} = \frac{1}{B} \sum_{k=1}^B \mu_{kj}, \quad (8)$$

$$\mu_{\text{std},j}^2 = \frac{1}{B} \sum_{k=1}^B \mu_{kj}^2 - \left(\frac{1}{B} \sum_{k=1}^B \mu_{kj} \right)^2, \quad (9)$$

$$\sigma_{\text{std},j}^2 = \frac{1}{B} \sum_{k=1}^B \sigma_{kj}^2 - \left(\frac{1}{B} \sum_{k=1}^B \sigma_{kj} \right)^2. \quad (10)$$

Encoding normalization is a modified form of batch normalization⁵⁶ for VAE latent spaces. As part of encoding normalization, we introduce a new hyperparameter, λ_{μ} , to scale the ratio of expectations $E(|\mu_{ij}|)/E(|\sigma_{ij}|)$. We use $\lambda_{\mu} = 2.5$ in this paper; however, we confirm that training is robust to values $\lambda_{\mu} \in \{1.0, 2.0, 2.5\}$ for a range of datasets and ANN architectures. Batch means are subtracted from μ and not σ as σ_{ij} should be positive. In addition, we multiply $\sigma_{\text{std},j}$ by an arbitrary factor of 2 so that $E(|\mu_{ij}|) \approx E(|\sigma_{ij}|)$ for $\lambda_{\mu} = 1$.

Encoding normalization enables the KL divergence loss in equation 5 to be removed as latent space regularization is built into the encoder architecture. However, we find that removing the KL loss can result in VAEs encoding either very low or very high σ_{ij} . In effect, an encoder can learn to use σ apply a binary mask to μ if a generator learns that latent features with very high absolute values are not meaningful. To prevent extreme σ_{ij} , we add a new encoding regularization loss, $\text{MSE}(\sigma, 1)$, to the encoder. Human vision is sensitive to edges⁶⁰, so we also add a gradient-based loss to improve realism. Adding a gradient-based loss is a computationally inexpensive alternative to training a VAE as part of a generative adversarial network⁶¹ (VAE-GAN) and often achieves similar performance. Our total training loss is

$$L = \lambda_{\text{MSE}} \text{MSE}(G(\mathbf{z}), I) + \lambda_{\text{Sobel}} \text{MSE}(S(G(\mathbf{z})), S(I)) + \text{MSE}(\sigma, 1), \quad (11)$$

where we chose $\lambda_{\text{MSE}} = \lambda_{\text{Sobel}} = 50$, and $S(x)$ computes a concatenation of horizontal and vertical Sobel derivatives⁶² of x . We found that training is robust to choices of $\lambda_{\text{MSE}} = \lambda_{\text{Sobel}}$ where $\lambda_{\text{MSE}} \text{MSE}(G(\mathbf{z}), I) + \lambda_{\text{Sobel}} \text{MSE}(S(G(\mathbf{z})), S(I))$ is in $[0.5, 25.0]$.

We trained VAEs to minimize L by ADAM⁶³ optimized stochastic gradient descent^{35,64}. At training iteration $t \in [1, T]$, we used a stepwise exponentially decayed learning rate⁶⁵,

$$\eta = \eta_{\text{start}} a^{\text{floor}(bt/T)}, \quad (12)$$

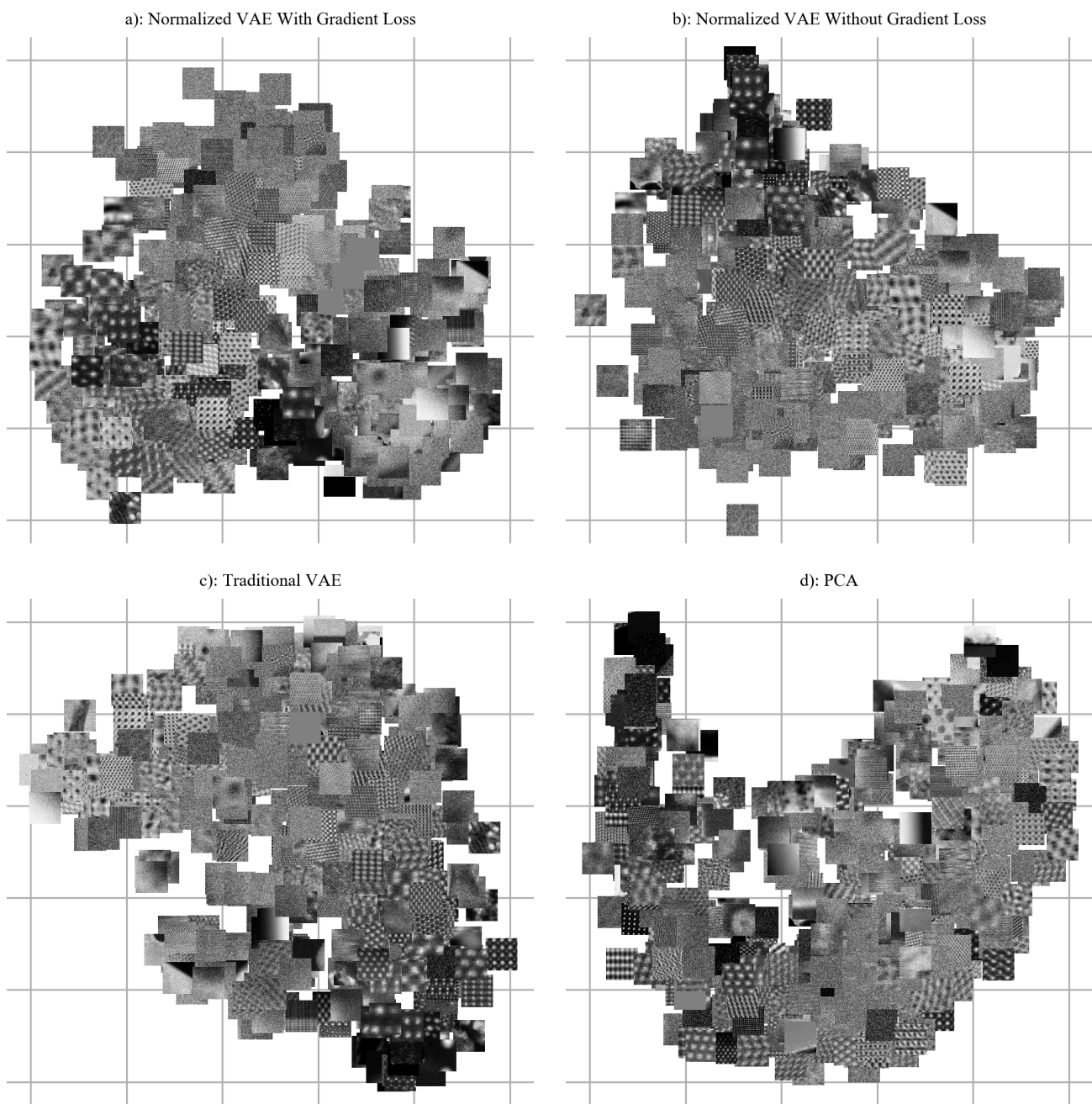


Figure 2. Images at 500 randomly selected images in two-dimensional tSNE visualizations of 19769 96×96 crops from STEM images for various embedding methods. Clustering improves in order a)→b)→c)→d).

and a DEMON⁶⁶ first moment of the momentum decay rate,

$$\beta_1 = \frac{\beta_{\text{start}}(1 - t/T)}{(1 - \beta_{\text{start}}) + \beta_{\text{start}}(1 - t/T)}, \quad (13)$$

where we chose initial values $\eta_{\text{start}} = 0.001$ and $\beta_{\text{start}} = 0.9$, exponential base $a = 0.5$, $b = 8$ steps, and $T = 600000$ iterations. We used a batch size of $B = 64$ and emphasize that a large batch size decreases complication of encoding normalization by varying batch statistics. Training our VAEs takes about 12 hours on a desktop computer with an Nvidia GTX 1080 Ti GPU and an Intel i7-6700 CPU.

To use VAE latent spaces to cluster data, means are often embedded by tSNE. However, this does not account for highly varying σ used to calculate latent features. To account for uncertainty, we modify calculation of pairwise similarities, p_{ij} , in equation 2 to include both μ_i and σ_i encoded for every example, $i \in [1, N]$, in our datasets,

$$p_{ij} = \exp\left(-\frac{1}{2\alpha_j^2} \sum_k w_{ijk} (\mu_{ik} - \mu_{jk})^2\right) \left(\sum_{m \neq j} \exp\left(-\frac{1}{2\alpha_j^2} \sum_k w_{mjk} (\mu_{mk} - \mu_{jk})^2\right)\right)^{-1}, \quad (14)$$

where we chose weights

$$w_{ijk} = \frac{1}{\sigma_{ik}^2 + \sigma_{jk}^2 + \varepsilon} \left(\sum_l \frac{1}{\sigma_{il}^2 + \sigma_{jl}^2 + \varepsilon}\right)^{-1}. \quad (15)$$

We add $\varepsilon = 0.01$ for numerical stability, and to account for uncertainty in σ due to encoder imperfections or variation in batch statistics. Following Oskolkov⁶⁷, we fit α_j to perplexities given by $N^{1/2}$, where N is the number of examples in a dataset, and confirm that changing perplexities by ± 100 has little effect on visualizations for our $N \simeq 20000$ TEM and STEM datasets. To ensure convergence, we run tSNE computations for 10000 iterations. In comparison, KL divergence is stable by 5000 iterations for our datasets. In preliminary experiments, we observe that tSNE with σ results in comparable visualizations to tSNE without σ , and we think that tSNE with σ may be a slight improvement. For comparison, pairs of visualizations with and without σ are indicated in supplementary information.

Our improvements to dataset visualization by tSNE are showcased in figure 2 for various embedding methods. The visualizations are for a new dataset containing 19769 96×96 crops from STEM images, which will be introduced in section 3. To suppress high-frequency noise during training, images were blurred by a 5×5 symmetric Gaussian kernel with a 2.5 px standard deviation. Clusters are most distinct in figure 2a for encoding normalized VAE training with a gradient loss described by equation 11. Ablating the gradient loss in figure 2b results in similar clustering; however, the VAE struggles to separate images of noise and fine atom columns. In contrast, clusters are not clearly separated in figure 2c for a traditional VAE described by equation 5. Finally, embedding the first 50 principal components extracted by a scikit-learn⁶⁸ implementation of probabilistic PCA in figure 2d does not result in clear clustering.

3 Scanning Transmission Electron Micrographs

We curated 19769 STEM images from University of Warwick electron microscopy dataservers to train ANNs for compressed sensing^{5,7}. Atom columns are visible in roughly two-thirds of images, and similar proportions are bright and dark field. In addition, most signals are noisy⁷⁵ and are imaged at several times their Nyquist rates⁷⁶. To reduce data transfer times for large images, we also created variant containing 161069 non-overlapping 512×512 crops from full images. For rapid development, we have also created new variants containing 96×96 images downsampled or cropped from full images. In this section we give details of each STEM dataset, referring to them using their names in our repositories.

STEM Full Images: 19769 32-bit TIFFs containing STEM images taken with a University of Warwick JEOL ARM 200F electron microscope by dozens of scientists working on hundreds of projects. Images were originally saved in DigitalMicrograph DM3 or DM4 files created by Gatan Microscopy Suite⁷⁷ software and have their original sizes and intensities. The dataset is partitioned into 14826 training, 1977 validation, and 2966 test set images. The dataset was made by concatenating contributions from different scientists, so partitioning the dataset before shuffling also partitions scientists.

STEM Crops: 161069 32-bit TIFFs containing 512×512 non-overlapping regions cropped from STEM Full Images. The dataset is partitioned into 110933 training, 21259 validation, and 28877 test set images. This dataset is biased insofar that larger images were divided into more crops.

STEM 96×96 : A 32-bit NumPy^{78,79} array with shape [19769, 96, 96, 1] containing 19769 STEM Full Images area downsampled to 96×96 with MATLAB and default antialiasing.

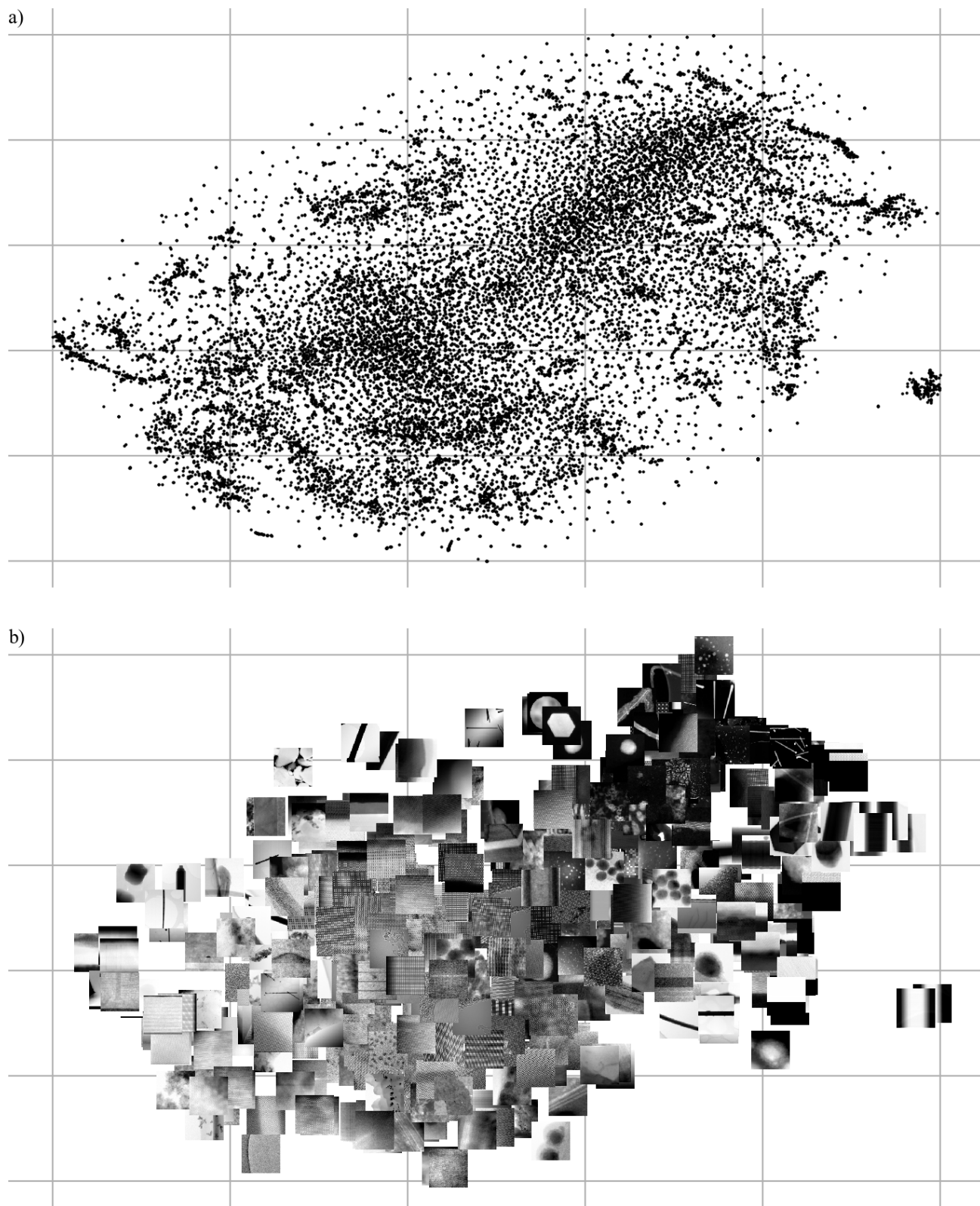


Figure 3. Two-dimensional tSNE visualization of 64-dimensional VAE latent spaces for 19769 STEM images that have been downsampled to 96×96 . The same grid is used to show a) map points and b) images at 500 randomly selected points.

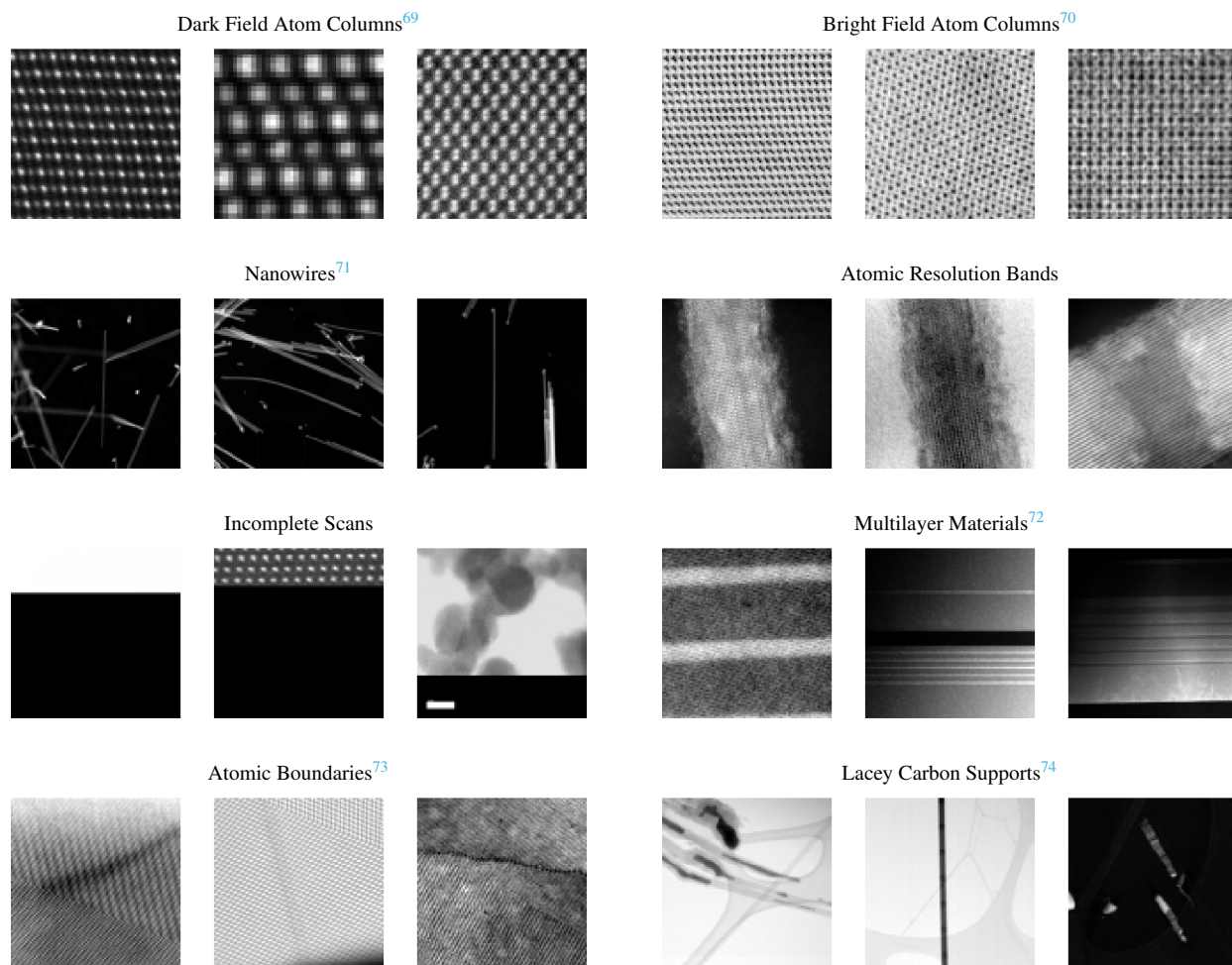


Table 1. Examples and descriptions of STEM images in our datasets. References put some images into context to make them more tangible to unfamiliar readers.

STEM 96×96 Crops: A 32-bit NumPy array with shape [19769, 96, 96, 1] containing 19769 96×96 regions cropped from STEM Full Images. Each crop is from a different image.

Variety of STEM 96×96 images is shown in figure 3 by clustering means and standard deviations of VAE latent spaces in two dimensions by tSNE. Details are in section 2. An interactive visualization that displays images when map points are hovered over is also available⁸. This paper is aimed at a general audience so readers may not be familiar with STEM. Subsequently, example images are tabulated with references and descriptions in table 1 to make them more tangible.

4 Transmission Electron Micrographs

We curated 17266 2048×2048 high-signal TEM images from University of Warwick electron microscopy dataservers to train ANNs to improve signal-to-noise⁴. However, our dataset was only available upon request. It is now openly available¹. For convenience, we have also created a new variant containing 96×96 images that can be used for rapid ANN development. In this section we give details of each TEM dataset, referring to them using their names in our repositories.

TEM Full Images: 17266 32-bit TIFFs containing 2048×2048 TEM images taken with University of Warwick JEOL 2000, JEOL 2100, JEOL 2100+, and JEOL ARM 200F electron microscope by dozens of scientists working on hundreds of projects. Images were originally saved in DigitalMicrograph DM3 or DM4 files created by Gatan Microscopy Suite⁷⁷ software and have been cropped to largest possible squares and area resized to 2048×2048 with MATLAB and default antialiasing. Images with at least 2500 electron counts per pixel were then linearly transformed to have minimum and maximum values of 0 and 1, respectively. We discarded images with less than 2500 electron counts per pixel as images were curated to train an electron

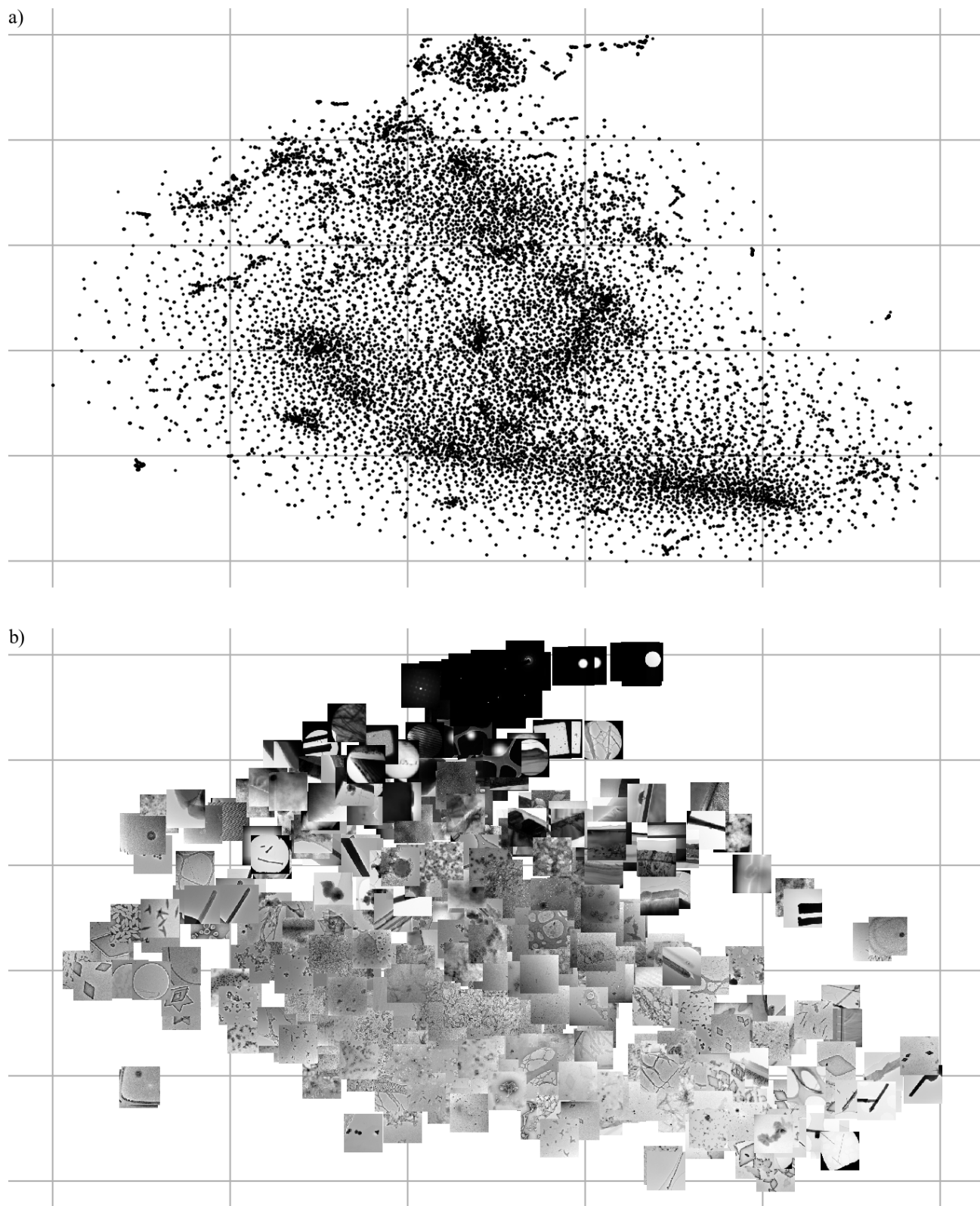


Figure 4. Two-dimensional tSNE visualization of 64-dimensional VAE latent spaces for 17266 TEM images that have been downsampled to 96×96 . The same grid is used to show a) map points and b) images at 500 randomly selected points.

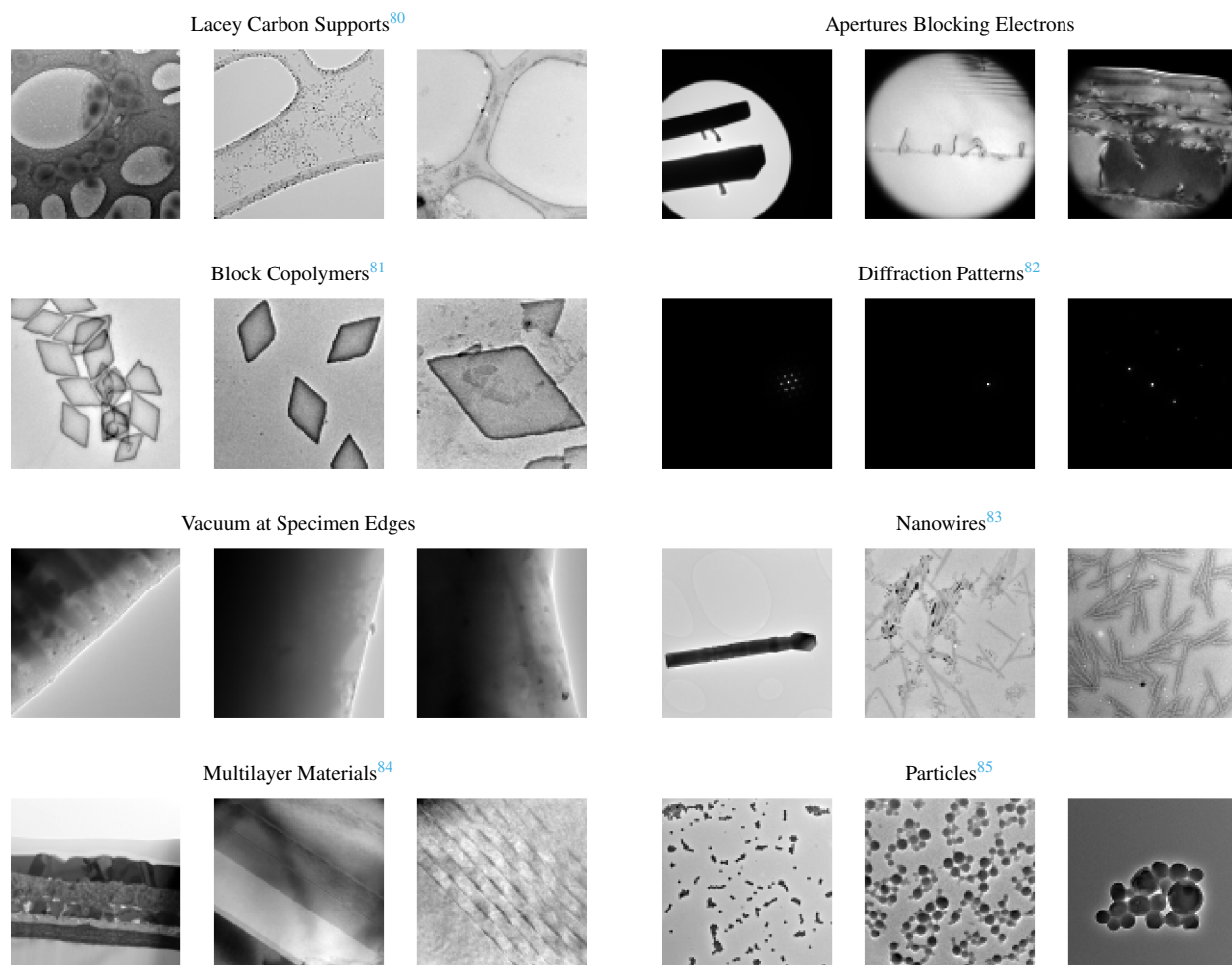


Table 2. Examples and descriptions of TEM images in our datasets. References put some images into context to make them more tangible to unfamiliar readers.

micrograph denoiser⁴. The dataset is partitioned into 11350 training, 2431 validation, and 3486 test set images. The dataset was made by concatenating contributions from different scientists, so each partition contains data collected by a different subset of scientists.

TEM 96×96: A 32-bit NumPy array with shape [17266, 96, 96, 1] containing 17266 TEM Full Images area downsampled to 96×96 with MATLAB and default antialiasing. Training, validation, and test set images are concatenated in that order.

Variety of TEM 96×96 images is shown in figure 4 by clustering means and standard deviations of VAE latent spaces in two dimensions by tSNE. Details are in section 2. An interactive visualization that displays images when map points are hovered over is also available⁸. This paper is aimed at a general audience so readers may not be familiar with TEM. Subsequently, example images are tabulated with references and descriptions in table 2 to make them more tangible.

5 Exit Wavefunctions

We simulated 98340 TEM exit wavefunctions to train ANNs to reconstruct phases from amplitudes³. Half of wavefunction information is undetected by conventional TEM as only the amplitude, and not the phase, of an image is recorded. Wavefunctions were simulated at 512×512 then centre-cropped to 320×320 to remove simulation edge artefacts. Wavefunctions have been simulated for real physics where Kirkland potentials⁸⁶ for each atom are summed from $n = 3$ terms, and by truncating Kirkland potential summations to $n = 1$ to simulate an alternative universe where atoms have different potentials. Wavefunctions simulated for an alternate universe can be used to test ANN robustness to simulation physics. For rapid development, we also downsampled $n = 3$ wavefunctions from 320×320 to 96×96. In this section we give details of each exit wavefunction dataset,

referring to them using their names in our repositories.

CIFs: 12789 CIFs downloaded from the Crystallography Open Database^{87–92} (COD). The CIFs are for materials published in inorganic chemistry journals. There are 150 New Journal of Chemistry, 1034 American Mineralogist, 1998 Journal of the American Chemical Society and 5457 Inorganic Chemistry CIFs used to simulate training set wavefunctions, 1216 Physics and Chemistry of Materials CIFs used to simulate validation set wavefunctions, and 2927 Chemistry of Materials CIFs used to simulate test set wavefunctions. In addition, the CIFs have been preprocessed to be input to cITEM wavefunction simulations.

URLs: COD Uniform Resource Locators⁹³ (URLs) that CIFs were downloaded from.

Wavefunctions: 36324 complex 64-bit NumPy files containing 320×320 wavefunctions. The wavefunctions are for a large range of materials and physical hyperparameters. The dataset is partitioned into 24530 training, 3399 validation, and 8395 test set wavefunctions. Metadata Javascript Object Notation⁹⁴ (JSON) files link wavefunctions to CIFs and contain some simulation hyperparameters.

Wavefunctions Unseen Training: 1544 64-bit NumPy files containing 320×320 wavefunctions. The wavefunctions are for training set CIFs and are for a large range of materials and physical hyperparameters. Metadata JSONs link wavefunctions to CIFs and contain some simulation hyperparameters.

Wavefunctions Single: 4825 complex 64-bit NumPy files containing 320×320 wavefunctions. The wavefunctions are for a single material, $\text{In}_{1.7}\text{K}_2\text{Se}_8\text{Sn}_{2.28}$ ⁹⁵, and a large range of physical hyperparameters. The dataset is partitioned into 3861 training, and 964 validation set wavefunctions. Metadata JSONs link wavefunctions to CIFs and contain some simulation hyperparameters.

Wavefunctions Restricted: 11870 complex 64-bit NumPy files containing 320×320 wavefunctions. The wavefunctions are for a large range of materials and a small range of physical hyperparameters. The dataset is partitioned into 8002 training, 1105 validation, and 2763 test set wavefunctions. Metadata JSON files link wavefunctions to CIFs and contain some simulation hyperparameters.

Wavefunctions 96×96 : A 32-bit NumPy array with shape [36324, 96, 96, 2] containing 36324 wavefunctions. The wavefunctions were simulated for a large range of materials and physical hyperparameters, and bilinearly downsampled with skimage⁴⁷ from 320×320 to 96×96 using default antialiasing. In Python⁹⁶, Real components are at index [...,0], and imaginary components are at index [...,1]. The dataset can be partitioned in 24530 training, 3399 validation, and 8395 test set wavefunctions, which have been concatenated in that order. To be clear, the training subset is at Python indexes [:24530].

Wavefunctions 96×96 Restricted: A 32-bit NumPy array with shape [11870, 96, 96, 2] containing 11870 wavefunctions. The wavefunctions were simulated for a large range of materials and a small range of physical hyperparameters, and bilinearly downsampled with skimage from 320×320 to 96×96 using default antialiasing. The dataset can be partitioned in 8002 training, 1105 validation, and 2763 test set wavefunctions, which have been concatenated in that order.

Wavefunctions 96×96 Single: A 32-bit NumPy array with shape [4825, 96, 96, 2] containing 11870 wavefunctions. The wavefunctions were simulated for $\text{In}_{1.7}\text{K}_2\text{Se}_8\text{Sn}_{2.28}$ and a large range of physical hyperparameters, and bilinearly downsampled with skimage from 320×320 to 96×96 using default antialiasing. The dataset can be partitioned in 3861 training, and 964 validation set wavefunctions, which have been concatenated in that order.

Wavefunctions $n = 1$: 37457 complex 64-bit NumPy files containing 320×320 wavefunctions. The wavefunctions are for a large range of materials and physical hyperparameters. The dataset is partitioned into 25352 training, 3569 validation, and 8563 test set wavefunctions. These wavefunctions are for an alternate universe where atoms have different potentials.

Wavefunctions $n = 1$ Unseen Training: 1501 64-bit NumPy files containing 320×320 wavefunctions. The wavefunctions are for training set CIFs and are for a large range of materials and physical hyperparameters. Metadata JSONs link wavefunctions to CIFs and contain some simulation hyperparameters. These wavefunctions are for an alternate universe where atoms have different potentials.

Wavefunctions $n = 1$ Single: 4819 complex 64-bit NumPy files containing 320×320 wavefunctions. The wavefunctions are for a single material, $\text{In}_{1.7}\text{K}_2\text{Se}_8\text{Sn}_{2.28}$, and a large range of physical hyperparameters. The dataset is partitioned into 3856 training, and 963 validation set wavefunctions. Metadata JSONs link wavefunctions to CIFs and contain some simulation hyperparameters. These wavefunctions are for an alternate universe where atoms have different potentials.

Experimental Focal Series: 1000 experimental focal series. Each series consists of 14 32-bit 512×512 TEM images, area downsampled from 4096×4096 with MATLAB and default antialiasing. The images are in TIFF⁹⁷ format. All series were created with a common, quadratically increasing⁹⁸ defocus series. However, spatial scales vary and would need to be fitted as part of wavefunction reconstruction.

In detail, exit wavefunctions for a large range of physical hyperparameters were simulated with cITEM^{99,100} for acceleration voltages in {80,200,300} kV, material depths uniformly distributed in [5,100) nm, material widths in [5,10) nm, and

crystallographic zone axes (h, k, l) $h, k, l \in \{0, 1, 2\}$. Materials were padded on all sides with vacuum 0.8 nm wide and 0.3 nm deep to reduce simulation artefacts. Finally, crystal tilts were perturbed by zero-centred Gaussian random variates with standard deviation 0.1° . We used default values for other cITEM hyperparameters. Simulations for a small range of physical hyperparameters used lower upper bounds that reduced simulation hyperparameter ranges by factors close to 1/4. All wavefunctions are linearly transformed to have a mean amplitude of 1.

All wavefunctions are for atom columns, so tSNE visualizations are provided in supplementary information to conserve space. The visualizations are for the Wavefunctions 96×96 , Wavefunctions 96×96 Restricted and Wavefunctions 96×96 Single datasets.

6 Discussion

The best dataset variant varies for different applications. Full-sized datasets can always be used as other dataset variants are derived from them. However, loading and processing full-sized examples may bottleneck training, and it is often unnecessary. Instead, smaller 512×512 crops, which can be loaded more quickly than the full-sized images, can often be used to train ANNs to be applied convolutionally¹⁰¹ to or tiled across⁴ full-sized inputs. In addition, our 96×96 datasets can be used for rapid initial development before scaling up to full-sized datasets, similar to how ANNs might be trained with CIFAR-10 before scaling up to ImageNet. However, subtle application- and dataset-specific considerations may also influence the best dataset choice. For example, an ANN trained with downsampled 96×96 inputs may not generalize to 96×96 crops from full-sized inputs as downsampling may introduce artifacts¹⁰² and change noise or other data characteristics.

In practice, electron microscopists image most STEM and TEM signals at several times their Nyquist rates⁷⁶. This eases visual inspection, decreases sub-Nyquist aliasing¹⁰³, improves display on computer monitors, and is easier than carefully tuning sampling rates to capture the minimum data needed to resolve signals. High sampling may also reveal additional high-frequency information when images are inspected after an experiment. However, this complicates ANN development as it means that information per pixel is often higher in downsampled images. For example, partial scans across STEM images that have been downsampled to 96×96 require higher coverages than scans across 96×96 crops for ANNs to learn to complete images with equal performance⁵. It also complicates the comparison of different approaches to compressed sensing. For example, we suggested that sampling 512×512 crops at a regular grid of probing locations outperforms sampling along spiral paths as a subsampling grid can still access most information⁵.

Test set performance should be calculated for a standardized dataset partition to ease comparison with other methods. Nevertheless, training and validation partitions can be varied to investigate validation variance for partitions with different characteristics. Default training and validation sets for STEM and TEM datasets contain contributions from different scientists that have been concatenated or numbered in order, so new validation partitions can be selected by concatenating training and validation partitions and moving the window used to select the validation set. Similarly, exit wavefunctions were simulated with CIFs from different journals that were concatenated or numbered sequentially. There is leakage^{104, 105} between training, validation and test sets due to overlap between materials published in different journals and between different scientists' work. However, further leakage can be minimized by selecting dataset partitions before any shuffling and, for wavefunctions, by ensuring that simulations for each journal are not split between partitions.

Experimental STEM and TEM image quality is variable. Images were taken by scientists with all levels of experience and TEM images were taken on multiple microscopes. This means that our datasets contain images that might be omitted from other datasets. For example, the tSNE visualization for STEM in figure 3 includes incomplete scans, ~ 50 blank images, and images that only contain noise. Similarly, the tSNE visualization for TEM in figure 4 revealed some images where apertures block electrons, and that there are small number of unprocessed standard diffraction and convergent beam electron diffraction¹⁰⁶ patterns. Although these conventionally low-quality images would not normally be published, they are important to ensure that ANNs are robust for live applications. In addition, inclusion of conventionally low-quality images may enable identification of this type of data. We encourage readers to try our interactive tSNE visualizations⁸ for detailed inspection of our datasets.

In this paper, we present tSNE visualizations of VAE latent spaces to show image variety. However, our VAEs can be directly applied to a wide range of additional applications. For example, successful tSNE clustering of latent spaces suggests that VAEs could be used to create a hash table^{107, 108} for an electron micrograph search engine. VAEs can also be applied to semantic manipulation¹⁰⁹, and clustering in tSNE visualizations may enable subsets of latent space that generate interesting subsets of data distributions to be identified. Other applications include using clusters in tSNE visualizations to label data for supervised learning, data compression, and anomaly detection^{110, 111}. To encourage further development, we have made our source code and pretrained VAEs openly available⁸.

7 Conclusion

We have provided details and visualizations for large new electron microscopy datasets that are publicly available in our new repositories. To create high-quality visualizations, we improved VAE training by introducing encoding normalization and regularization, and an image gradient loss. In addition, we propose a new tSNE loss that accounts for both the means and standard deviations of VAE latent spaces. Datasets have been carefully partitioned into training, validation, and test sets for machine learning. In addition to full-sized datasets, we have provided variants containing 512×512 crops to reduce data loading times, and examples downsampled to 96×96 for rapid development. Source code, pretrained VAEs, precompiled tSNE binaries, and interactive dataset visualizations are provided in supplementary repositories to help users become familiar with our datasets and visualizations. By making our datasets available, we aim to encourage standardization of performance benchmarks in electron microscopy and increase participation of the wider computer science community in electron microscopy research.

8 Supplementary Information

Note: Content in this section will be provided in a supplementary document with the published version of this manuscript.

Ten additional tSNE visualizations are provided as supplementary information. They are for:

- Extracting 50 principal components by probabilistic PCA for the STEM 96×96 , STEM 96×96 Crops, TEM 96×96 , Wavefunctions 96×96 , Wavefunctions 96×96 Restricted and Wavefunctions 96×96 Single datasets. PCA is a quick and effective method to extract features. As a result, we think that visualizations for PCA are interesting benchmarks.
- VAE latent spaces with σ propagation for the STEM 96×96 Crops dataset. Crops show smaller features than downsampled images.
- VAE latent spaces without σ propagation for the STEM 96×96 , STEM 96×96 Crops and TEM 96×96 datasets. They are comparable to visualizations created with σ propagation.

Interactive versions of tSNE visualizations that display data when map points are hovered over are available⁸ for every figure. In addition, we propose an algorithm to increase whitespace utilization in tSNE visualizations by uniformly separating points.

9 Data Availability

The data that support the findings of this study are openly available at <https://doi.org/10.5281/zenodo.3834197>. For additional information contact the corresponding author (J.M.E.).

References

1. Ede, J. M. Electron Microscopy Datasets. Online: <https://github.com/Jeffrey-Ede/datasets/wiki> (2020).
2. FEI Company. An Introduction to Electron Microscopy. Online: <https://www.fei.com/documents/introduction-to-microscopy-document> (2010).
3. Ede, J. M., Peters, J. J. P., Sloan, J. & Beanland, R. Exit Wavefunction Reconstruction from Single Transmission Electron Micrographs with Deep Learning. *arXiv preprint arXiv:2001.10938* (2020).
4. Ede, J. M. & Beanland, R. Improving Electron Micrograph Signal-to-Noise with an Atrous Convolutional Encoder-Decoder. *Ultramicroscopy* **202**, 18–25 (2019).
5. Ede, J. M. & Beanland, R. Partial Scanning Transmission Electron Microscopy with Deep Learning. *arXiv preprint arXiv:1910.10467* (2020).
6. Ede, J. M. & Beanland, R. Adaptive Learning Rate Clipping Stabilizes Learning. *Mach. Learn. Sci. Technol.* **1**, 015011, DOI: [10.1088/2632-2153/ab81e2](https://doi.org/10.1088/2632-2153/ab81e2) (2020).
7. Ede, J. M. Deep Learning Supersampled Scanning Transmission Electron Microscopy. *arXiv preprint arXiv:1910.10467* (2019).
8. Ede, J. M. Dataset Preparation and Visualization. Online: <https://github.com/Jeffrey-Ede/datasets> (2020).
9. Schmidt, J., Marques, M. R., Botti, S. & Marques, M. A. Recent Advances and Applications of Machine Learning in Solid-State Materials Science. *npj Comput. Mater.* **5**, 1–36 (2019).
10. von Lilienfeld, O. A. Introducing Machine Learning: Science and Technology. *Mach. Learn. Sci. Technol.* **1**, 010201 (2020).

11. Belianinov, A. *et al.* Big Data and Deep Data in Scanning and Electron Microscopies: Deriving Functionality from Multidimensional Data Sets. *Adv. Struct. Chem. Imaging* **1**, 1–25 (2015).
12. Hornik, K., Stinchcombe, M. & White, H. Multilayer Feedforward Networks are Universal Approximators. *Neural Networks* **2**, 359–366 (1989).
13. Lin, H. W., Tegmark, M. & Rolnick, D. Why does Deep and Cheap Learning Work so Well? *J. Stat. Phys.* **168**, 1223–1247 (2017).
14. Raschka, S. Model Evaluation, Model Selection, and Algorithm Selection in Machine Learning. *arXiv preprint arXiv:1811.12808* (2018).
15. Roh, Y., Heo, G. & Whang, S. E. A Survey on Data Collection for Machine Learning: A Big Data-AI Integration Perspective. *IEEE Transactions on Knowl. Data Eng.* (2019).
16. Hall, S. R., Allen, F. H. & Brown, I. D. The Crystallographic Information File (CIF): A New Standard Archive File for Crystallography. *Acta Crystallogr. Sect. A: Foundations Crystallogr.* **47**, 655–685 (1991).
17. Baker, M. Reproducibility Crisis? *Nature* **533**, 353–66 (2016).
18. Hutson, M. Artificial Intelligence Faces Reproducibility Crisis (2018).
19. Iudin, A., Korir, P. K., Salavert-Torres, J., Kleywegt, G. J. & Patwardhan, A. EMPIAR: A Public Archive for Raw Electron Microscopy Image Data. *Nat. Methods* **13**, 387 (2016).
20. Hey, T., Butler, K., Jackson, S. & Thiyagalingam, J. Machine Learning and Big Scientific Data. *Philos. Transactions Royal Soc. A* **378**, 20190054 (2020).
21. Krizhevsky, A., Nair, V. & Hinton, G. The CIFAR-10 Dataset. Online: <http://www.cs.toronto.edu/~kriz/cifar.html> (2014).
22. Krizhevsky, A. & Hinton, G. Learning Multiple Layers of Features from Tiny Images. Tech. Rep., Citeseer (2009).
23. LeCun, Y., Cortes, C. & Burges, C. MNIST Handwritten Digit Database. AT&T Labs, Online: <http://yann.lecun.com/exd/b/mnist> (2010).
24. Russakovsky, O. *et al.* ImageNet Large Scale Visual Recognition Challenge. *Int. J. Comput. Vis.* **115**, 211–252 (2015).
25. Tenenbaum, J. B., De Silva, V. & Langford, J. C. A Global Geometric Framework for Nonlinear Dimensionality Reduction. *Science* **290**, 2319–2323 (2000).
26. Roweis, S. T. & Saul, L. K. Nonlinear Dimensionality Reduction by Locally Linear Embedding. *science* **290**, 2323–2326 (2000).
27. Zhang, Z. & Wang, J. MLL: Modified Locally Linear Embedding Using Multiple Weights. In *Advances in Neural Information Processing Systems*, 1593–1600 (2007).
28. Donoho, D. L. & Grimes, C. Hessian Eigenmaps: Locally Linear Embedding Techniques for High-Dimensional Data. *Proc. Natl. Acad. Sci.* **100**, 5591–5596 (2003).
29. Belkin, M. & Niyogi, P. Laplacian Eigenmaps for Dimensionality Reduction and Data Representation. *Neural Comput.* **15**, 1373–1396 (2003).
30. Zhang, Z. & Zha, H. Principal Manifolds and Nonlinear Dimensionality Reduction via Tangent Space Alignment. *SIAM J. on Sci. Comput.* **26**, 313–338 (2004).
31. Buja, A. *et al.* Data Visualization with Multidimensional Scaling. *J. Comput. Graph. Stat.* **17**, 444–472 (2008).
32. Van Der Maaten, L. Accelerating t-SNE Using Tree-Based Algorithms. *The J. Mach. Learn. Res.* **15**, 3221–3245 (2014).
33. Maaten, L. v. d. & Hinton, G. Visualizing Data Using t-SNE. *J. Mach. Learn. Res.* **9**, 2579–2605 (2008).
34. Wattenberg, M., Viégas, F. & Johnson, I. How to Use t-SNE Effectively. *Distill* **1**, e2 (2016).
35. Ruder, S. An Overview of Gradient Descent Optimization Algorithms. *arXiv preprint arXiv:1609.04747* (2016).
36. Schubert, E. & Gertz, M. Intrinsic t-Stochastic Neighbor Embedding for Visualization and Outlier Detection. In *International Conference on Similarity Search and Applications*, 188–203 (Springer, 2017).
37. Halko, N., Martinsson, P.-G. & Tropp, J. A. Finding Structure with Randomness: Probabilistic Algorithms for Constructing Approximate Matrix Decompositions. *SIAM Rev.* **53**, 217–288 (2011).
38. Martinsson, P.-G., Rokhlin, V. & Tygert, M. A Randomized Algorithm for the Decomposition of Matrices. *Appl. Comput. Harmon. Analysis* **30**, 47–68 (2011).

39. Wall, M. E., Rechtsteiner, A. & Rocha, L. M. Singular Value Decomposition and Principal Component Analysis. In *A Practical Approach to Microarray Data Analysis*, 91–109 (Springer, 2003).
40. Jolliffe, I. T. & Cadima, J. Principal Component Analysis: A Review and Recent Developments. *Philos. Transactions Royal Soc. A: Math. Phys. Eng. Sci.* **374**, 20150202 (2016).
41. Dalal, N. & Triggs, B. Histograms of Oriented Gradients for Human Detection. In *2005 IEEE Computer Society Conference on Computer Vision and Pattern Recognition (CVPR'05)*, vol. 1, 886–893 (IEEE, 2005).
42. Bay, H., Ess, A., Tuytelaars, T. & Van Gool, L. Speeded-Up Robust Features (SURF). *Comput. Vis. Image Underst.* **110**, 346–359 (2008).
43. Ojala, T., Pietikainen, M. & Maenpaa, T. Multiresolution Gray-Scale and Rotation Invariant Texture Classification with Local Binary Patterns. *IEEE Transactions on pattern analysis machine intelligence* **24**, 971–987 (2002).
44. Mallat, S. G. A Theory for Multiresolution Signal Decomposition: The Wavelet Representation. *IEEE Transactions on Pattern Analysis Mach. Intell.* **11**, 674–693 (1989).
45. Latif, A. *et al.* Content-Based Image Retrieval and Feature Extraction: A Comprehensive Review. *Math. Probl. Eng.* **2019** (2019).
46. Minka, T. P. Automatic Choice of Dimensionality for PCA. In *Advances in Neural Information Processing Systems*, 598–604 (2001).
47. Van der Walt, S. *et al.* scikit-image: Image Processing in Python. *PeerJ* **2**, e453 (2014).
48. Tschannen, M., Bachem, O. & Lucic, M. Recent Advances in Autoencoder-Based Representation Learning. *arXiv preprint arXiv:1812.05069* (2018).
49. Kramer, M. A. Nonlinear Principal Component Analysis Using Autoassociative Neural Networks. *AIChE J.* **37**, 233–243 (1991).
50. Marcelino, P. Transfer Learning From Pre-trained Models. Towards Data Science, online: <https://towardsdatascience.com/transfer-learning-from-pre-trained-models-f2393f124751> (2018).
51. Ede, J. M. Kernels, MLPs and Autoencoders. Online: <https://github.com/Jeffrey-Ede/Denoising-Kernels-MLPs-Autoencoders> (2018).
52. Ede, J. M. Autoencoders, Kernels, and Multilayer Perceptrons for Electron Micrograph Restoration and Compression. *arXiv preprint arXiv:1808.09916* (2018).
53. Kingma, D. P. & Welling, M. Auto-Encoding Variational Bayes. *arXiv preprint arXiv:1312.6114* (2014).
54. McCann, M. T., Jin, K. H. & Unser, M. Convolutional Neural Networks for Inverse Problems in Imaging: A Review. *IEEE Signal Process. Mag.* **34**, 85–95 (2017).
55. Krizhevsky, A., Sutskever, I. & Hinton, G. E. ImageNet Classification with Deep Convolutional Neural Networks. In *Advances in Neural Information Processing Systems*, 1097–1105 (2012).
56. Ioffe, S. & Szegedy, C. Batch Normalization: Accelerating Deep Network Training by Reducing Internal Covariate Shift. *arXiv preprint arXiv:1502.03167* (2015).
57. Nair, V. & Hinton, G. E. Rectified Linear Units Improve Restricted Boltzmann Machines. In *Proceedings of the 27th International Conference on Machine Learning (ICML-10)*, 807–814 (2010).
58. Higgins, I. *et al.* beta-VAE: Learning Basic Visual Concepts with a Constrained Variational Framework. *Int. Conf. on Learn. Represent.* **2**, 6 (2017).
59. Hu, Q. & Greene, C. S. Parameter Tuning is a Key Part of Dimensionality Reduction via Deep Variational Autoencoders for Single Cell RNA Transcriptomics. In *Pacific Symposium on Biocomputing. Pacific Symposium on Biocomputing*, vol. 24, 362 (NIH Public Access, 2019).
60. McIlhagga, W. Estimates of Edge Detection Filters in Human Vision. *Vis. research* **153**, 30–36 (2018).
61. Larsen, A. B. L., Sønderby, S. K., Larochelle, H. & Winther, O. Autoencoding Beyond Pixels using a Learned Similarity Metric. *arXiv preprint arXiv:1512.09300* (2015).
62. Vairalkar, M. K. & Nimbhorkar, S. Edge Detection of Images using Sobel Operator. *Int. J. Emerg. Technol. Adv. Eng.* **2**, 291–293 (2012).
63. Kingma, D. P. & Ba, J. ADAM: A Method for Stochastic Optimization. *arXiv preprint arXiv:1412.6980* (2014).

64. Zou, D., Cao, Y., Zhou, D. & Gu, Q. Stochastic Gradient Descent Optimizes Over-Parameterized Deep ReLU Networks. *arXiv preprint arXiv:1811.08888* (2018).
65. Ge, R., Kakade, S. M., Kidambi, R. & Netrapalli, P. The Step Decay Schedule: A Near Optimal, Geometrically Decaying Learning Rate Procedure. *arXiv preprint arXiv:1904.12838* (2019).
66. Chen, J. & Kyrillidis, A. Decaying Momentum Helps Neural Network Training. *arXiv preprint arXiv:1910.04952* (2019).
67. Oskolkov, N. How to Tune Hyperparameters of tSNE. Towards Data Science, Online: <https://towardsdatascience.com/how-to-tune-hyperparameters-of-tsne-7c0596a18868> (2019).
68. Pedregosa, F. *et al.* Scikit-learn: Machine Learning in Python. *J. Mach. Learn. Res.* **12**, 2825–2830 (2011).
69. Van den Bos, K. H. *et al.* Unscrambling Mixed Elements Using High Angle Annular Dark Field Scanning Transmission Electron Microscopy. *Phys. Rev. Lett.* **116**, 246101 (2016).
70. Zhou, D. *et al.* Sample Tilt Effects on Atom Column Position Determination in ABF-STEM Imaging. *Ultramicroscopy* **160**, 110–117 (2016).
71. Bu, L. *et al.* Surface Engineering of Hierarchical Platinum-Cobalt Nanowires for Efficient Electrocatalysis. *Nat. Commun.* **7**, 1–10 (2016).
72. Monclús, M. *et al.* Effect of Layer Thickness on the Mechanical Behaviour of Oxidation-Strengthened Zr/Nb Nanoscale Multilayers. *J. Mater. Sci.* **53**, 5860–5878 (2018).
73. Pyrz, W. D. *et al.* Atomic-Level Imaging of Mo-VO Complex Oxide Phase Intergrowth, Grain Boundaries, and Defects Using HAADF-STEM. *Proc. Natl. Acad. Sci.* **107**, 6152–6157 (2010).
74. McGilvery, C. M., Goode, A. E., Shaffer, M. S. & McComb, D. W. Contamination of Holey/Lacey Carbon Films in STEM. *Micron* **43**, 450–455 (2012).
75. Seki, T., Ikuhara, Y. & Shibata, N. Theoretical Framework of Statistical Noise in Scanning Transmission Electron Microscopy. *Ultramicroscopy* **193**, 118–125 (2018).
76. Landau, H. Sampling, Data Transmission, and the Nyquist Rate. *Proc. IEEE* **55**, 1701–1706 (1967).
77. Gatan Microscopy Suite. Online: www.gatan.com/products/tem-analysis/gatan-microscopy-suite-software (2019).
78. NPY Format. Online: <https://docs.scipy.org/doc/numpy/reference/generated/numpy.lib.format.html> (2019).
79. Kern, R. NEP 1 — A Simple File Format for NumPy Arrays. Online: <https://numpy.org/neps/nep-0001-npy-format.html> (2007).
80. Karlsson, G. Thickness Measurements of Lacey Carbon Films. *J. Microsc.* **203**, 326–328 (2001).
81. Inam, M. *et al.* 1D vs. 2D Shape Selectivity in the Crystallization-Driven Self-Assembly of Polylactide Block Copolymers. *Chem. Sci.* **8**, 4223–4230 (2017).
82. Bendersky, L. A. & Gayle, F. W. Electron Diffraction Using Transmission Electron Microscopy. *J. Res. Natl. Inst. Standards Technol.* **106**, 997 (2001).
83. Wu, Y., Messer, B. & Yang, P. Superconducting MgB₂ Nanowires. *Adv. Mater.* **13**, 1487–1489 (2001).
84. Pang, B. *et al.* The Microstructural Characterization of Multiferroic LaFeO₃-YMnO₃ Multilayers Grown on (001)- and (111)-SrTiO₃ Substrates by Transmission Electron Microscopy. *Materials* **10**, 839 (2017).
85. Dong, Z. *et al.* Individual Particles of Cryoconite Deposited on the Mountain Glaciers of the Tibetan Plateau: Insights into Chemical Composition and Sources. *Atmospheric Environ.* **138**, 114–124 (2016).
86. Kirkland, E. J. *Advanced Computing in Electron Microscopy* (Springer Science & Business Media, 2010).
87. Quirós, M., Gražulis, S., Girdzijauskaitė, S., Merkys, A. & Vaitkus, A. Using SMILES Strings for the Description of Chemical Connectivity in the Crystallography Open Database. *J. Cheminformatics* **10**, DOI: [10.1186/s13321-018-0279-6](https://doi.org/10.1186/s13321-018-0279-6) (2018).
88. Merkys, A. *et al.* COD::CIF::Parser: An Error-Correcting CIF Parser for the Perl Language. *J. Appl. Crystallogr.* **49**, DOI: [10.1107/S1600576715022396](https://doi.org/10.1107/S1600576715022396) (2016).
89. Gražulis, S., Merkys, A., Vaitkus, A. & Okulič-Kazarinas, M. Computing Stoichiometric Molecular Composition From Crystal Structures. *J. Appl. Crystallogr.* **48**, 85–91, DOI: [10.1107/S1600576714025904](https://doi.org/10.1107/S1600576714025904) (2015).
90. Gražulis, S. *et al.* Crystallography Open Database (COD): An Open-Access Collection of Crystal Structures and Platform for World-Wide Collaboration. *Nucleic Acids Res.* **40**, D420–D427, DOI: [10.1093/nar/gkr900](https://doi.org/10.1093/nar/gkr900) (2012). <http://nar.oxfordjournals.org/content/40/D1/D420.full.pdf+html>.

91. Gražulis, S. *et al.* Crystallography Open Database – An Open-Access Collection of Crystal Structures. *J. Appl. Crystallogr.* **42**, 726–729, DOI: [10.1107/S0021889809016690](https://doi.org/10.1107/S0021889809016690) (2009).
92. Downs, R. T. & Hall-Wallace, M. The American Mineralogist Crystal Structure Database. *Am. Mineral.* **88**, 247–250 (2003).
93. Berners-Lee, T., Masinter, L. & McCahill, M. RFC1738: Uniform Resource Locators (URL). *RFC* DOI: [10.17487/RFC1738](https://doi.org/10.17487/RFC1738) (1994).
94. ISO/IEC JTC 1/SC 22. International Standard ISO/IEC21778: Information Technology - The JSON Data Interchange Syntax. Online: <https://www.iso.org/standard/71616.html> (2017).
95. Hwang, S.-J., Iyer, R. G., Trikalitis, P. N., Ogden, A. G. & Kanatzidis, M. G. Cooling of Melts: Kinetic Stabilization and Polymorphic Transitions in the KInSnSe₄ System. *Inorg. chemistry* **43**, 2237–2239 (2004).
96. Python Software Foundation. Python 3.6. Online: <http://www.python.org> (2020).
97. Adobe Developers Association *et al.* TIFF Revision 6.0. Online: www.adobe.io/content/dam/udp/en/open/standards/tiff/TIFF6.pdf (1992).
98. Haigh, S., Jiang, B., Alloyeau, D., Kisielowski, C. & Kirkland, A. Recording Low and High Spatial Frequencies in Exit Wave Reconstructions. *Ultramicroscopy* **133**, 26–34 (2013).
99. Peters, J. J. P. & Dyson, M. A. cITEM. Online: <https://github.com/JJPPeters/cITEM> (2019).
100. Dyson, M. A. *Advances in Computational Methods for Transmission Electron Microscopy Simulation and Image Processing*. Ph.D. thesis, University of Warwick (2014).
101. Zhu, J.-Y., Park, T., Isola, P. & Efros, A. A. Unpaired Image-to-Image Translation Using Cycle-Consistent Adversarial Networks. In *Proceedings of the IEEE International Conference on Computer Vision*, 2223–2232 (2017).
102. MicroImages. Resampling Methods. Technical Guide, Online: <https://www.microimages.com/documentation/TechGuide/s/77resampling.pdf> (2010).
103. Amidror, I. Sub-Nyquist Artefacts and Sampling Moiré Effects. *Royal Soc. Open Sci.* **2**, 140550 (2015).
104. Open Data Science. How to Fix Data Leakage - Your Model's Greatest Enemy. Towards Data Science, online: <https://medium.com/@ODSC/how-to-fix-data-leakage-your-models-greatest-enemy-e34fa26abac5> (2019).
105. Bussola, N., Marcolini, A., Maggio, V., Jurman, G. & Furlanello, C. Not Again! Data Leakage in Digital Pathology. *arXiv preprint arXiv:1909.06539* (2019).
106. Tanaka, M. Convergent-Beam Electron Diffraction. *Acta Crystallogr. Sect. A: Foundations Crystallogr.* **50**, 261–286 (1994).
107. Patterson, N. & Wang, Y. Semantic Hashing with Variational Autoencoders.
108. Jin, G., Zhang, Y. & Lu, K. Deep Hashing Based on VAE-GAN for Efficient Similarity Retrieval. *Chin. J. Electron.* **28**, 1191–1197 (2019).
109. Klys, J., Snell, J. & Zemel, R. Learning Latent Subspaces in Variational Autoencoders. In *Advances in Neural Information Processing Systems*, 6444–6454 (2018).
110. Yao, R., Liu, C., Zhang, L. & Peng, P. Unsupervised Anomaly Detection Using Variational Auto-Encoder based Feature Extraction. In *2019 IEEE International Conference on Prognostics and Health Management (ICPHM)*, 1–7 (IEEE, 2019).
111. Xu, H. *et al.* Unsupervised Anomaly Detection via Variational Auto-Encoder for Seasonal KPIs in Web Applications. In *Proceedings of the 2018 World Wide Web Conference*, 187–196 (2018).

10 Acknowledgements

Funding: J.M.E. acknowledges EPSRC EP/N035437/1 and EPSRC Studentship 1917382.

11 Competing Interests

The author declares no competing interests.